Accepted Manuscript

Informed constrained spherical deconvolution (iCSD)

Timo Roine, Ben Jeurissen, Daniele Perrone, Jan Aelterman, Wilfried Philips, Alexander Leemans, Jan Sijbers

PII: S1361-8415(15)00008-0
DOI: http://dx.doi.org/10.1016/j.media.2015.01.001
Reference: MEDIMA 963

To appear in: *Medical Image Analysis*

Received Date: 18 April 2014
Revised Date: 22 December 2014
Accepted Date: 5 January 2015

Please cite this article as: Roine, T., Jeurissen, B., Perrone, D., Aelterman, J., Philips, W., Leemans, A., Sijbers, J., *Informed* constrained spherical deconvolution (iCSD), *Medical Image Analysis* (2015), doi: http://dx.doi.org/10.1016/j.media.2015.01.001

Informed constrained spherical deconvolution (iCSD)

Timo Roine[a,*], Ben Jeurissen[a], Daniele Perrone[b], Jan Aelterman[b], Wilfried Philips[b], Alexander Leemans[c], Jan Sijbers[a]

[a] *iMinds-Vision Lab, Department of Physics, University of Antwerp, Antwerp, Belgium*
[b] *Ghent University-iMinds/Image Processing and Interpretation, Ghent, Belgium*
[c] *Image Sciences Institute, University Medical Center Utrecht, Utrecht, The Netherlands*

Abstract

Diffusion-weighted (DW) magnetic resonance imaging (MRI) is a noninvasive imaging method, which can be used to investigate neural tracts in the white matter (WM) of the brain. However, the voxel sizes used in DW-MRI are relatively large, making DW-MRI prone to significant partial volume effects (PVE). These PVEs can be caused both by complex (e.g. crossing) WM fiber configurations and non-WM tissue, such as gray matter (GM) and cerebrospinal fluid. High angular resolution diffusion imaging methods have been developed to correctly characterize complex WM fiber configurations, but significant non-WM PVEs are also present in a large proportion of WM voxels.

In constrained spherical deconvolution (CSD), the full fiber orientation distribution function (fODF) is deconvolved from clinically feasible DW data using a response function (RF) representing the signal of a single coherently oriented population of fibers. Non-WM PVEs cause a loss of precision in the detected fiber orientations and an emergence of false peaks in CSD, more prominently in voxels with GM PVEs. We propose a method, *informed* CSD (iCSD), to improve the estimation of fODFs under non-WM PVEs by modifying the RF to account for non-WM PVEs locally. In practice, the RF is modified based on tissue fractions estimated from high-resolution anatomical data.

Results from simulation and in-vivo bootstrapping experiments demonstrate a significant improvement in the precision of the identified fiber orientations and in the number of false peaks detected under GM PVEs. Probabilistic whole brain tractography shows fiber density is increased in the major WM tracts and decreased in subcortical GM regions. The iCSD method significantly improves the fiber orientation estimation at the WM-GM inter-

face, which is especially important in connectomics, where the connectivity between GM regions is analyzed.

Keywords: diffusion MRI, fiber orientation, response function, partial volume effect, constrained spherical deconvolution, tractography, connectomics, gray matter

1. Introduction

Diffusion-weighted (DW[1]) magnetic resonance imaging (MRI) is a non-invasive imaging method to investigate tissue microstructure via the measurement of the displacement of water molecules (Stejskal and Tanner, 1965; Jones, 2010). Diffusion in white matter (WM) neural tracts is anisotropic, larger parallel to the tract than perpendicular to it. This property can be exploited to extract fiber orientations from DW data and investigate neural tracts in the brain WM using fiber tractography algorithms (Conturo et al., 1999; Basser et al., 2000; Mori and van Zijl, 2002; Jones, 2008; Tournier et al., 2010; Jeurissen et al., 2011).

The image resolution in DW-MRI is relatively low, with voxel sizes typically larger than $2 \times 2 \times 2$ mm^3. Thus, significant partial volume effects (PVE) are present in the measured DW signal (Alexander et al., 2001; Vos

*Corresponding author:
Timo Roine
iMinds-Vision Lab, Department of Physics
University of Antwerp
Universiteitsplein 1, Building N
2610 Wilrijk (Antwerp), Belgium
Email address: timo.roine@uantwerpen.be (Timo Roine)

[1] **Abbreviations**: ACT: anatomically constrained tractography, CI: confidence interval, CSD: constrained spherical deconvolution, CSF: cerebrospinal fluid, DTI: diffusion tensor imaging, DSI: diffusion spectrum imaging, DW: diffusion-weighted, EPI: echo-planar imaging, FA: fractional anisotropy, fODF: fiber orientation distribution function, FOV: field of view, FWE: free water elimination, GM: gray matter, HARDI: high angular resolution diffusion imaging, iCSD: informed constrained spherical deconvolution, MD: mean diffusivity, MPRAGE: magnetization-prepared rapid gradient-echo, MRI: magnetic resonance imaging, NEX: number of excitations, PVE: partial volume effect, RF: response function, SH: spherical harmonics, SNR: signal-to-noise ratio, TDI: tract-density imaging, VF: volume fraction, WM: white matter

et al., 2011). These PVEs may be caused by complex WM fiber configurations, such as crossing tracts (Vos et al., 2011; Jeurissen et al., 2013), or several tissue types present in a voxel (Pasternak et al., 2009; Metzler-Baddeley et al., 2012b; Roine et al., 2014a).

Currently, the most common method to analyze DW-MRI data is diffusion tensor imaging (DTI) (Basser et al., 1994b,a; Jones and Leemans, 2011; Tournier et al., 2011). However, its shortcoming is the inability to identify complex fiber configurations (Alexander et al., 2001; Frank, 2001, 2002), present in 60–90 % of WM voxels (Jeurissen et al., 2013). To overcome this, high angular resolution diffusion imaging (HARDI) (Tuch et al., 2002; Jansons and Alexander, 2003; Tournier et al., 2004; Tuch, 2004; Anderson, 2005; Alexander, 2005; Hosey et al., 2005; Tournier et al., 2007; Dell'Acqua et al., 2007; Descoteaux et al., 2007; Behrens et al., 2007; Descoteaux et al., 2009; Daducci et al., 2014) and methods based on diffusion spectrum imaging (DSI) (Wedeen et al., 2005, 2008; Canales-Rodríguez et al., 2010) have been developed.

However, although able to identify complex fiber configurations, many of the HARDI methods do not account for PVEs caused by non-WM tissue, such as gray matter (GM) and cerebrospinal fluid (CSF) (Dell'Acqua et al., 2010; Metzler-Baddeley et al., 2012b; Roine et al., 2014a). In our previous study, we reported that significant PVEs with non-WM tissue were present in 35–50 % of WM voxels, of which the vast majority was with GM (Roine et al., 2014a). This indicates that the non-WM PVEs are nearly as common as complex fiber configurations within a voxel, and thus taking them into account is important.

Diffusion in non-WM tissue is mostly isotropic within the resolution of DW-MRI (Dell'Acqua et al., 2010). Isotropic non-WM PVEs have been shown to affect DTI (Alexander et al., 2001; Pasternak et al., 2009; Metzler-Baddeley et al., 2012b) and constrained spherical deconvolution (CSD) (Tournier et al., 2007; Roine et al., 2014a). Pasternak et al. (2009) used constrained optimization of a bi-tensor model for free water elimination (FWE) in DTI, showing increased fractional anisotropy (FA) and mean diffusivity (MD). Metzler-Baddeley et al. (2012b) used FWE to correct for CSF-contamination in tensor-derived measures in CSD-based tractography and showed that diffusivity measures were more sensitive to PVEs than anisotropy measures. However, FWE-based approaches are not suitable for GM-contaminated regions. Roine et al. (2014a) showed that in CSD, the precision of the identified fiber orientations decreased and the number of spurious false peaks increased,

when isotropic non-WM volume fraction (VF) increased. These effects were most prominent with GM, which may cause significant consequences when studying the connectivity between GM regions.

In HARDI methods, few methods account for non-WM PVEs. To the authors' knowledge, the ball and stick model is one of the few methods that directly includes an isotropic compartment and has been extended into multiple fiber orientations (Behrens et al., 2003, 2007; Schultz et al., 2010; Jbabdi et al., 2012). In addition, a method based on total variation and sparse deconvolution has been developed to address the isotropic partial volume effects in q-ball imaging (Tuch, 2004; Zhou et al., 2014). In another study, isotropic non-WM PVEs were dampened through adaptive regularization in the iterative Richardson-Lucy deconvolution algorithm (Dell'Acqua et al., 2010). This method reduced the number of spurious false peaks, but is limited in that it reports large isotropic fODFs in regions without WM fibers.

CSD is currently one of the most used, clinically feasible and readily available HARDI methods (Tournier et al., 2012; Leemans et al., 2009; Metzler-Baddeley et al., 2012a; Emsell et al., 2013; Farquharson et al., 2013; Forde et al., 2013; Kristo et al., 2013; McGrath et al., 2013a,b; Reijmer et al., 2013b,a; Thompson et al., 2014; Roine et al., 2014b). In CSD, the fiber orientation distribution function (fODF) is estimated from clinically feasible DW data by deconvolving the data with a kernel constructed from a response function (RF) representing a single coherently oriented population of fibers (Tournier et al., 2004, 2007). However, the non-WM PVEs have not previously been taken into account in CSD.

In this paper, we propose a novel method, *informed* CSD (iCSD), where the traditional RF representing a single fiber orientation in pure WM regions is modified to account for isotropic diffusion from GM and CSF. In practice, this can be done by using VFs estimated from high-resolution anatomical data. We evaluate the performance of the proposed method in comparison to the original CSD with comprehensive simulations. In addition, experiments on real DW data are performed to confirm the simulation results.

2. Material and methods

We propose a novel method to improve the fiber orientation estimation with CSD under non-WM PVEs. The performance of the method is evaluated with simulations and in-vivo experiments.

2.1. Fiber orientation estimation with CSD

In CSD, the full fODF is deconvolved from the DW signal using a kernel constructed from the RF representing a single coherently oriented population of WM fibers (Tournier et al., 2004). During the deconvolution procedure, to be able to reliably solve the ill-posed problem, constraints are imposed to suppress negative peaks in the fODF (Tournier et al., 2007, 2008). The RF is the DW signal of an ideal fiber population perfectly aligned along the z-axis. In practice, it can be estimated from real data by recursive calibration (Tax et al., 2014) or by selecting voxels with high FA, (e.g. FA $>$ 0.7), aligning their principal eigenvectors along the z-axis, and then averaging their spherical harmonics (SH) decompositions (Tournier et al., 2004).

2.2. Informed CSD (iCSD)

In WM regions with non-WM PVEs, the use of the single traditional RF estimated from pure WM voxels is not accurate. Therefore, we propose a novel method, iCSD, which exploits the VFs estimated from high-resolution T1-weighted data to account for local non-WM PVEs in CSD. In iCSD, the RF corresponding to a single coherently oriented population of fibers is adapted to the local tissue composition. This anatomically-informed RF is estimated by linearly combining the DW signal from the WM RF with the isotropic RFs from GM or CSF tissue, assuming no exchange between the compartments, as shown in Figure 1. Thus, the RF in iCSD becomes:

$$\mathbf{r}_{\mathrm{iCSD}} = f_{\mathrm{wm}}\mathbf{r}_{\mathrm{wm}} + f_{\mathrm{gm}}\mathbf{r}_{\mathrm{gm}} + f_{\mathrm{csf}}\mathbf{r}_{\mathrm{csf}}, \tag{1}$$

where $\mathbf{r}_{\mathrm{iCSD}}$ is the iCSD RF, $\mathbf{r}_{\mathrm{wm}}$ is the single-fiber RF from pure WM tissue (as in CSD), f_{wm}, f_{gm} and f_{csf} are the VFs of WM, GM and CSF tissue and $\mathbf{r}_{\mathrm{gm}}$ and $\mathbf{r}_{\mathrm{csf}}$ are the isotropic GM and CSF responses, respectively.

After the deconvolution with the iCSD RF, the resulting fODF is proportional to the WM volume in the voxel. However, as the fODF was extracted from the voxels with different tissue types, a scaling factor of f_{wm} should be used to scale the amplitudes of the fODF to be proportional to the total volume of the voxel.

2.3. Simulated DW data

The WM signal was simulated for two crossing WM fiber configurations with equal weight, FA, and MD. The orientation of the first fiber bundle was

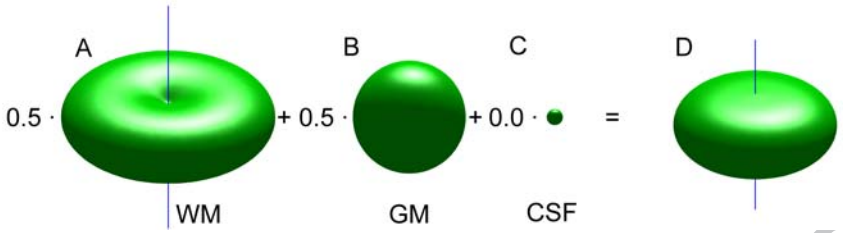

Figure 1: An illustration of the proposed anatomically-informed response function (RF) estimation with an example tissue composition of 50 % WM, 50 % GM and 0 % CSF. The traditional RF corresponding to a single fiber orientation in pure WM voxels (A) is combined with the GM (B) and CSF (C) RFs based on volume fractions estimated from high-resolution T1-weighted data. Thus, an anatomically-informed RF (D) is received, which is more accurately adapted to the local tissue composition.

randomly selected, after which the orientation of the second fiber bundle was calculated in spherical coordinates with a predefined crossing angle.

Then, the DW signal was simulated separately for different tissue types, and the resulting signals were combined assuming no exchange between the compartments (Leemans et al., 2005). The number of gradient directions uniformly distributed on the unit half-sphere was 64 (Jones et al., 1999). To avoid any bias caused by the gradient orientations, a different gradient set was used for each simulated DW signal. The signals from the specific WM fiber configurations were combined with isotropic CSF and GM compartments. Based on Basser and Jones (2002), the combined simulated DW signal $S(\mathbf{b})$ for a single gradient orientation corresponding to $\mathbf{b}$ is:

$$\begin{aligned} S(\mathbf{b}) = & f_{\text{wm}}(f_{\text{fiber1}}e^{-\text{Trace}(\mathbf{bD}_{\text{fiber1}})} + f_{\text{fiber2}}e^{-\text{Trace}(\mathbf{bD}_{\text{fiber2}})}) \\ & + f_{\text{gm}}e^{-\text{Trace}(\mathbf{bD}_{\text{gm}})} + f_{\text{csf}}e^{-\text{Trace}(\mathbf{bD}_{\text{csf}})}, \end{aligned} \tag{2}$$

where f_{fiber1} and f_{fiber2} are the VFs of the two fibers with respect to the WM compartment, and $\mathbf{D}_{\text{fiber1}}$ and $\mathbf{D}_{\text{fiber2}}$ are the diffusion tensors of the fibers (FA=0.8, MD=0.0007 mm^2/s), and $\mathbf{D}_{\text{gm}}$ and $\mathbf{D}_{\text{csf}}$ are the isotropic tensors of the DW signal in GM (FA=0, MD=0.0007 mm^2/s) and CSF (FA=0, MD=0.002 mm^2/s), respectively. Complex Gaussian noise was added to the combined DW signal, resulting in Rician distributed data.

In the simulations, the iCSD RF can be calculated using the diffusion tensors of the respective compartments and the following formula (Basser and Jones, 2002):

$$r_{\text{s}}(\mathbf{b}) = f_{\text{wm}}e^{-\text{Trace}(\mathbf{bD}_{\text{wm}})} + f_{\text{gm}}e^{-\text{Trace}(\mathbf{bD}_{\text{gm}})} + f_{\text{csf}}e^{-\text{Trace}(\mathbf{bD}_{\text{csf}})}, \tag{3}$$

where $r_s(\mathbf{b})$ is the amplitude of the simulated iCSD RF along the single gradient orientation corresponding to $\mathbf{b}$, the b-matrix summarizing the interactions of all gradient waveforms applied in the acquisition (Mattiello et al., 1997). $\mathbf{D}_{wm}$ is the diffusion tensor of the DW signal in single-fiber WM voxels (FA=0.8, MD=0.0007 mm^2/s). Complex Gaussian noise is added, with a signal-to-noise ratio (SNR) equal to the simulated signal, resulting in Rician distributed data. SNR is calculated with respect to the non-diffusion weighted signal in pure WM (Dietrich et al., 2007; Tournier et al., 2013).

2.4. Extraction of peak measures from the fODFs

To find the peaks of the fODF estimated with CSD from both simulated and in-vivo DW data, a Newton optimization algorithm was used to extract the local maxima of the fODF directly based on the SH decompositions (Jeurissen et al., 2013). Optimization was initialized on a dense set of uniformly distributed spherical sample points (Jones et al., 1999). A threshold of 33 % of the maximum amplitude and 0.1 absolute amplitude of the fODF was used to discard small peaks, as commonly used in tractography (Tournier et al., 2010; Jeurissen et al., 2011; Tournier et al., 2012). A maximum of 6 of the highest peaks were identified. The peaks were clustered around the peaks of the average fODF calculated over all simulation repetitions performed with the same parameter configuration. Peaks further away than half of the crossing angle (with an upper limit of 35 degrees) from any of the peaks of the average fODF were not included in the clusters. A mean dyadic tensor was used to derive the average orientation for each of the identified fiber clusters (Basser and Pajevic, 2000; Jones, 2003). This orientation was then compared to the true orientations of the simulated fiber bundles to calculate bias. Peaks in clusters that were less than half of the crossing angle (with an upper limit of 35 degrees) from the true orientations were considered true peaks, and the rest of the peaks, including those not assigned to a cluster, false peaks. From the true clusters, accuracy (bias) and precision (95^{th} percentile confidence interval, CI) with respect to the orientation of the mean dyadic tensor were calculated.

2.5. Simulation experiments

Simulation experiments were conducted to study the performance of CSD with the modified RF in comparison to the original RF. Simulations and

analyses were performed in Matlab (The MathWorks, Inc., Natick, Massachusetts, United States), by using dedicated software programmed by the authors.

Precision, accuracy, and the number of correct and false peaks identified were investigated under GM and CSF PVEs varying the non-WM VF from 0.00 to 0.95. The angle between the fiber configurations was varied from 40 to 90 degrees, and the b-value from 1000 to 3500 s/mm^2. The SNR, calculated with respect to the non-diffusion weighted signal in pure WM, was varied from 10 to 60. We performed 1000 repetitions for each parameter configuration by adding different realizations of Rician noise to the simulated DW signal. The fODFs were estimated from the simulated DW signals with CSD using an SH representation truncated at orders from 4 to 14. Both the original RF and the anatomically-informed RF, as explained in section 2.2, were used in the estimation of the fODFs. The individual peaks and quantitative measures were extracted from the fODFs according to section 2.4.

To study the effect of each parameter separately in the simulations, only one parameter at a time was varied. The default values for the non-varying parameters were: b-value: 3000 s/mm^2; angle between the crossing fiber configurations: 70 degrees; SNR: 20 (as measured in real data). The default maximum SH order was 8.

2.6. Data acquisition and pre-processing

High angular resolution DW data were acquired on a 3T MRI system with a 32-channel head coil. The healthy volunteer gave written informed consent to participate in this study under a protocol approved by the local ethics committee. A single-shot echo-planar imaging (EPI) sequence was used with TR=8100 ms, TE=116 ms and 2.5 $\times$ 2.5 $\times$ 2.5 mm^3 voxel size. The field of view (FOV) was 240 $\times$ 240 mm^2 with a 96 $\times$ 96 acquisition matrix and the number of excitations (NEX) was 1. In the axial direction, 54 slices were imaged with 2.5 mm thickness and no gap. Diffusion sensitizing gradients with b = 2800 s/mm^2 were applied along 75 non-collinear directions. Ten images without diffusion-weighting (b = 0 s/mm^2) were acquired, of which one was acquired with reverse phase-encoding for the purpose of the EPI distortion correction. The SNR of the non-DW images was calculated to be approximately 20 in WM tissue using the method presented by Dietrich et al. (2007) and Tournier et al. (2013). High-resolution anatomical T1-weighted images were acquired with a 3D magnetization-prepared rapid gradient-echo (MPRAGE) sequence (Mugler and Brookeman, 1990) with TR=1900 ms,

TE=2.52 ms, TI=900 ms and $1 \times 1 \times 1$ mm^3 voxel size (flip angle = 9° and NEX = 1). FOV was $250 \times 250 \times 176$ mm^3 with a $256 \times 256 \times 176$ acquisition matrix.

The DW data were corrected for subject motion and eddy current induced distortions (Andersson et al., 2012; Leemans and Jones, 2009) and FMRIB Software Library's (FSL) TOPUP was used to correct for EPI distortions (Andersson et al., 2003). Four tissue types (CSF, cortical GM, deep GM and WM) were segmented on the structural image using the state-of-the-art framework outlined in Smith et al. (2012). In summary, the approach combines several tools from the FSL, including the Brain Extraction Tool (BET) (Smith, 2002), the FMRIB Automated Segmentation Tool (FAST) (Zhang et al., 2001), and the FMRIB Integrated Registration and Segmentation Tool (FIRST) (Patenaude et al., 2011), to obtain a reliable partial volume fraction map for all four tissue types. The structural data was aligned to the DW images using rigid body registration in SPM (Ashburner and Friston, 2003) (http://www.fil.ion.ucl.ac.uk/spm/software/spm8/). The MRtrix package (J-D Tournier, Brain Research Institute, Melbourne, Australia, https://github.com/jdtournier/mrtrix3) was used for probabilistic tractography and visualization of the in-vivo experiments (Tournier et al., 2012).

2.7. In-vivo fODF bootstrapping

The precision of the extracted fiber orientations was evaluated in in-vivo data by using residual bootstrapping in combination with SH modeling to create different realizations from the DW data of a single subject (Jeurissen et al., 2011). Thus, the same voxels between the different realizations can be directly compared to each other, which is not possible when using different acquisitions, even of the same subject. The residuals were calculated by subtracting the SH decomposition, using up to 8$^{\text{th}}$ order terms, of the DW signal from the original signal and they were corrected for leverage (Jeurissen et al., 2011; Davison and Hinkley, 1997). Then, 200 realizations of the DW data were generated, by randomly choosing with replacement among the residuals and adding the bootstrapped residuals to the SH decomposition of the original DW signal.

The fODFs from the different realizations were extracted with CSD and iCSD using up to 8$^{\text{th}}$ order SH. The peaks of the fODFs and quantitative measures were extracted as explained in section 2.4, with the exception that a constant threshold of 20 degrees was used in the clustering of the peaks. The precision (95$^{\text{th}}$ percentile CI) of the identified peaks (in a cluster) and

the number of unstable peaks (not in a cluster) were calculated. The term unstable peaks was chosen, as it refers to these peaks not being found reliably across the 200 bootstrap realizations of the same voxel.

2.8. In-vivo tractography

To investigate the effect of the proposed method on tractography performed based on the fODFs, we performed probabilistic whole brain tractography with the iFOD2 algorithm (Tournier et al., 2010, 2012). Tract-density imaging (TDI) was used to investigate the differences between the reconstructed tractograms (Calamante et al., 2010). The difference between the TDIs derived using iCSD and CSD was calculated (iCSD − CSD), which resulted in an image indicating whether there are more tracts passing through each voxel using the original CSD or iCSD approaches.

3. Results

The results of the fODF estimation using the proposed iCSD method in comparison to the original CSD implementation are presented in this section. Experiments with simulated as well as in-vivo data are presented. In addition, the effects of the proposed method on probabilistic tractography are presented.

3.1. Simulation experiments

Figure 2 shows the effect of isotropic non-WM volume using iCSD and original CSD. The proposed method significantly increased the precision (Fig. 2B) and reduced the number of false peaks (Fig. 2D) with both CSF and GM PVEs. The improvement was more prominent with GM PVEs. However, the method had a small negative effect on accuracy (Fig. 2A). The number of correct peaks detected decreased with very high isotropic VFs (Fig. 2C), which was more clearly expressed with CSF PVEs. The results with SH orders 8 (Fig. 2A-D) and 12 (Fig. 2E-H) were similar.

The effect of varying non-WM volume with a lower diffusion-weighting of b = 1000 s/mm^2 is shown in Figure 3. The isotropic PVEs can now be seen in lower non-WM fractions and the performance of both the proposed iCSD and original CSD methods was worse than with the high b-value of b = 3000 s/mm^2. The proposed method could not distinguish the two correct fiber orientations under very high (larger than 0.85) non-WM fractions, which caused also an increase in bias. However, until volume fractions of 0.6–0.8,

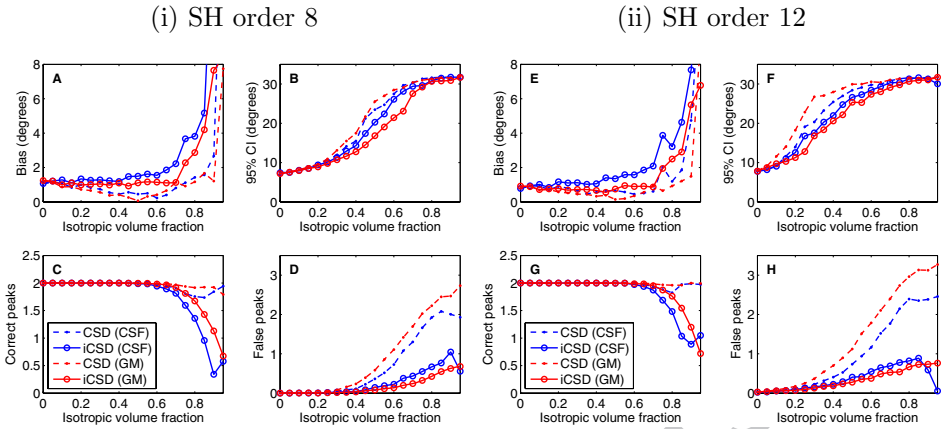

Figure 2: Bias, 95 % confidence interval (CI), and the number of correct and false peaks estimated using iCSD and original CSD as a function VF of CSF and GM. Figures A-D with SH order 8 and E-H with SH order 12 (diffusion weighting 3000 s/mm^2, angle 70 degrees, and SNR 20).

the proposed method increased the precision and reduced the number of spurious false peaks, with only a small 1–2 degree increase in bias.

The trends of the different methods were similar with different b-values, as shown in Figure 4. The precision remained significantly higher and the number of false peaks was close to zero with 50% non-WM VFs using all b-values. The bias of the proposed method was slightly increased, approximately one degree higher for all b-values.

The effect of different maximum SH orders is shown in Figure 5. The estimation with the proposed method resulted in increased precision and decreased number of false peaks in comparison to the original method with SH orders of 6 or larger.

The effect of different SNRs is shown in Figure 6. Figures 4A-D show the results with 50 % and Figures 4E-H with 75 % non-WM VF. With the original CSD, the results under high GM PVEs (75 %) did not improve with SNR. However, with the proposed iCSD method the precision increased in the case of large PVEs, and the number of false peaks remained lower than with original CSD. A slight decrease in the number of correct peaks can be noticed with the proposed method at very low SNR.

The effect of the varying angle between the fiber configurations is shown in Figure 7. The number of false peaks for the iCSD was lower for all angles

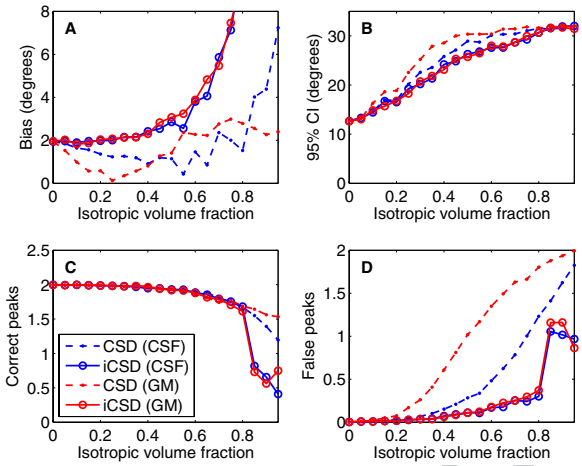

Figure 3: Bias (A), 95 % confidence interval (CI) (B), and the number of correct (C) and false peaks (D) estimated using iCSD and original CSD as a function VF of CSF and GM (diffusion weighting 1000 s/mm^2, SH order 8, angle 70 degrees, and SNR 20).

and the precision was improved for angles larger than 50 degrees. For the 50 degree crossing, the number of correct peaks was slightly lower than with the original method. The 40 degree crossing could not be identified correctly under 50 % non-WM VF with either of the methods.

An example of the fODFs estimated with iCSD and original CSD methods is shown in Figure 8. The default parameter values were used. The blue lines correspond to the true orientations. With the original method, small false peaks appeared with 40 % GM VF and significant deviation from the true orientations was present with 60-80 % VFs. The proposed method could detect the two fiber orientation correctly and without any false peaks until 60 % VFs, but a deviation from the true orientations was present with 80 % VF.

3.2. In-vivo fODF bootstrapping

Voxel-wise measures for the precision (95 % CI) and the number of unstable peaks were derived from real data based on 200 realizations generated by bootstrapping the residuals of the SH decomposition. The measures as a function of non-WM VF are presented in Figure 9. In addition, coronal, sagittal and axial illustrations for the differences in these measures are provided in Figure 10. The differences were calculated by subtracting the

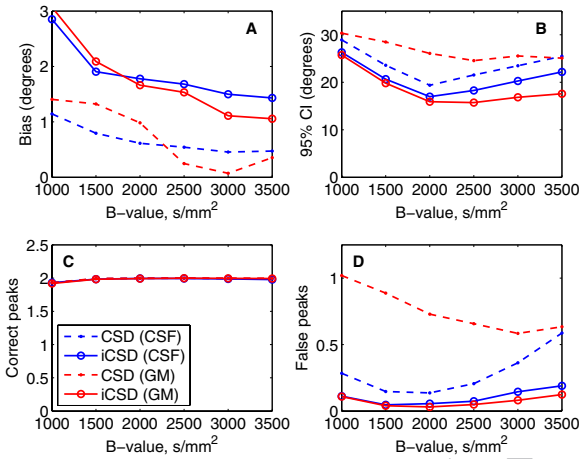

Figure 4: Bias (A), 95 % confidence interval (CI) (B), and the number of correct (C) and false peaks (D) estimated using iCSD and original CSD as a function of b-value (with 50% isotropic VF, SH order 8, angle 70 degrees, and SNR 20).

measures estimated with the original CSD method from the ones estimated with the iCSD approach. Thus, a negative value indicates that the measured quantity is lower for the proposed method.

The improvement in precision (95 % CI), as shown in Figure 9, was statistically significant for GM VFs larger than or equal to 25 %. For the number of unstable peaks, significance was reached already with 15 % GM VF. Statistical significance was tested with a two-tailed two-sample t-test assuming unequal variances, and Bonferroni correction for multiple comparisons was used to control for familywise error rate. The total number of statistical tests performed was 80 and thus, the significance threshold (for $\alpha = 0.05$) is $p < 0.000625$. The p-values, t-values and the number of voxels for each VF configuration are presented in Table 1, and the significant p-values after Bonferroni correction are marked with an asterisk. For CSF, no statistical significance was reached in the individual VF measures, partly due to less voxels being affected by CSF PVEs. In addition, the global measures over all voxels with significant non-WM PVEs (25 % – 75 % non-WM and at least 25 % WM) were calculated. Of these global measures, both the increase in precision and the decrease in the number of unstable peaks with iCSD were statistically significant for GM PVEs, and the number of unstable peaks was significantly reduced also for CSF PVEs.

	GM					CSF				
		95 % CI		Unstable peaks			95 % CI		Unstable peaks	
VF	N	t-stat	p-value	t-stat	p-value	N	t-stat	p-value	t-stat	p-value
5 %	2393	0.921	0.993	2.56	0.787	284	0.067	0.993	0.181	0.787
10 %	1923	2.21	0.357	4.58	1.04E-02	200	0.109	0.947	0.096	0.856
15 %	1612	3.31	2.71E-02	5.32	4.89E-06*	139	0.189	0.914	0.222	0.924
20 %	1640	3.72	9.39E-04	8.27	1.12E-07*	135	0.128	0.851	0.296	0.824
25 %	1638	4.94	2.04E-04*	9.49	1.91E-16*	125	0.375	0.898	0.196	0.767
30 %	1630	6.28	8.31E-07*	10.8	4.14E-21*	107	0.222	0.708	0.572	0.845
35 %	1678	6.60	3.80E-10*	14.0	1.24E-26*	113	0.524	0.824	0.116	0.568
40 %	1683	8.14	4.65E-11*	16.3	2.22E-43*	112	0.273	0.601	0.237	0.908
45 %	1648	9.13	5.46E-16*	19.1	8.75E-58*	101	0.441	0.785	0.632	0.813
50 %	1630	10.4	1.15E-19*	21.8	4.67E-77*	111	0.414	0.659	0.808	0.528
55 %	1597	12.4	5.85E-25*	25.7	2.11E-98*	117	0.351	0.680	0.830	0.420
60 %	1482	13.0	9.37E-35*	29.3	1.76E-132*	112	0.550	0.726	0.613	0.407
65 %	1306	14.0	1.07E-37*	32.7	5.45E-166*	115	0.735	0.583	1.18	0.540
70 %	1315	15.2	4.95E-43*	39.9	6.32E-197*	105	0.751	0.463	1.55	0.237
75 %	1271	17.4	3.60E-50*	47.6	2.73E-270*	118	0.570	0.454	1.01	0.122
80 %	1356	21.9	1.30E-63*	57.5	0*	132	0.871	0.569	2.77	0.315
85 %	1463	25.6	2.73E-97*	60.2	0*	164	0.200	0.385	1.27	6.02E-03
90 %	1535	29.2	3.35E-127*	38.2	0*	209	1.12	0.841	2.01	0.207
95 %	1932	35.5	1.06E-153*	15.4	3.26E-234*	251	-1.70	0.264	-1.05	4.55E-02
25%–75%	14776	31.4	5.70E-213*	68.5	0*	342	2.84	4.66E-03	6.07	2.14E-09*

Table 1: Statistical tests for the precision (95 % CI) and the number of unstable peaks for different GM and CSF VFs.

VF: volume fraction, N: number of voxels, GM: gray matter, CSF: cerebrospinal fluid, CI: confidence interval. Statistically significant differences (after Bonferroni correction) are marked with *.

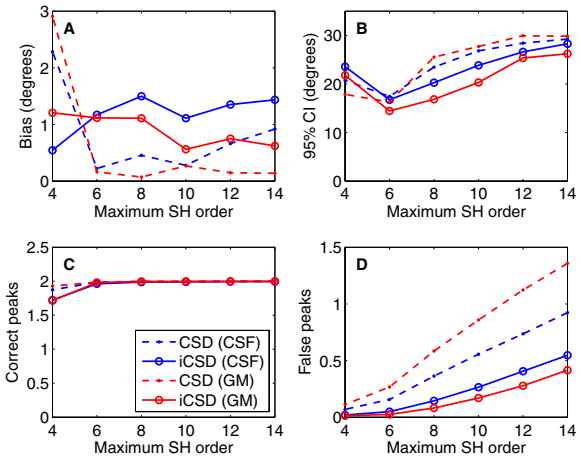

Figure 5: Bias (A), 95 % confidence interval (CI) (B), and the number of correct (C) and false peaks (D) estimated using iCSD and original CSD as a function of SH order (with 50% isotropic VF, diffusion weighting 3000 s/mm^2, angle 70 degrees, and SNR 20).

Example fODFs from the lateral occipital cortex, near the Brodmann area 19 are presented in Figure 11. The original fODFs are presented on the left and the iCSD fODFs on the right, visualized on the WM tissue fraction map (white = 100 % WM, black = 0% WM). In addition, the differences in precision and in the number of unstable peaks are presented below the estimated fODFs. Another example region in the occipital lobe is shown in Figure 12. The area in question is marked with a red rectangle, and the fODFs estimated with the CSD and iCSD methods are visualized on the WM VF map. Both of the example regions show large changes in the fODFs, most clearly expressed as the reduction in the number of spurious peaks and the decrease of the fiber amplitudes, due to the non-WM signal removed from the voxel. In addition, the precision is improved and the number of unstable peaks reduced, as shown in Figure 11 (*iii* and *iv*).

3.3. In-vivo tractography

Probabilistic whole brain tractography indicated that there are small differences in the reconstructed tracts between iCSD and original CSD. These differences were the most pronounced in the major WM tracts and their cortical extensions, where the tract density was increased and in the deep gray matter, where the density was decreased with iCSD in comparison to

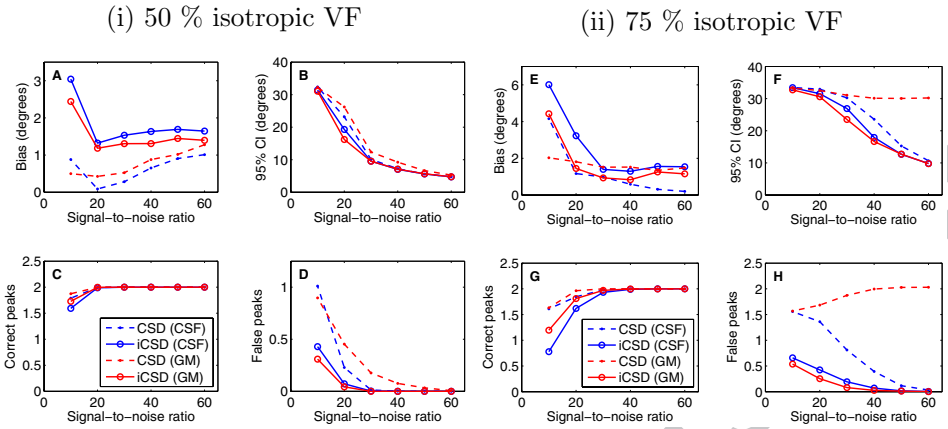

Figure 6: Bias, 95 % confidence interval (CI), and the number of correct and false peaks estimated using iCSD and original CSD as a function of SNR (using SH order 8, diffusion weighting 3000 s/mm^2, angle 70 degrees). Figures A-D with 50 % and E-H with 75 % isotropic VF.

the original CSD method. An illustration of these differences is provided in Figure 13.

4. Discussion

We proposed a method, iCSD, to improve the reliability of fiber orientation estimation in CSD for regions under non-WM PVEs by modifying the RF used in the estimation of the fODF to account for local tissue composition. The results showed a significant improvement compared to the original CSD in the precision of the identified fiber orientations and in the number of spurious false peaks detected under GM PVEs both in simulated and real DW data. A small decrease in accuracy is present in the simulation results, but the bias is small while the increase in precision and the reduction in the number of false peaks are much more pronounced.

Our previous results indicated that although CSD is efficient and accurate in the detection of complex fiber configurations within a voxel, precision of the estimated fiber orientations decreases and the number of false peaks detected increases in the case of GM contamination, which was estimated to be present in 35-50 % of WM voxels (Roine et al., 2014a). This will most likely introduce false positives and hinder tract propagation into the cortex or near subcortical GM tissue. Reliable tractography at the WM-

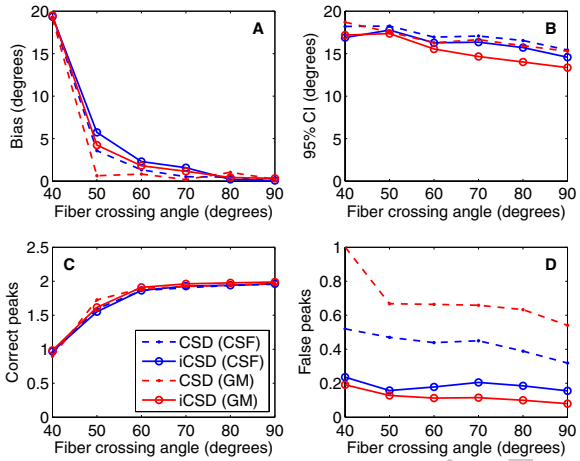

Figure 7: Bias (A), 95 % confidence interval (CI) (B), and the number of correct (C) and false peaks (D) estimated using iCSD and original CSD as a function of the angle between the fiber configurations (with 50% isotropic VF, diffusion weighting 3000 s/mm^2, SH order 8, and SNR 20). To be able to compare the measures, a constant angular threshold was used (20 degrees) in the clustering.

GM interface is especially important in connectomics, where the connectivity between GM regions is analyzed. An algorithm, anatomically constrained tractography (ACT), already exists (Smith et al., 2012). In ACT, tracts are discarded based on their anatomical feasibility and thus, only tracts that correctly propagate to the cortex are accepted. However, the problem of false positives and systematic errors in the tractography performed based on erroneous fODFs remains. Therefore, we decided to develop a method to take these non-WM PVEs into account directly in the estimation of fODFs in CSD and thus, potentially improve the accuracy of tractography in the regions under GM contamination. The proposed method does not guarantee the anatomical feasibility of the tracts, and it may be used in conjunction with ACT (Smith et al., 2012).

Part of the non-WM PVEs is due to the reduced SNR of the WM compartment, which can not be recovered. The rest of the effects are caused by the mostly isotropic diffusion from the non-WM tissue. This is shown in the difference between the measures of GM and CSF VFs. As shown in Roine et al. (2014a), CSF signal is completely attenuated with b-values from 1500–2000 s/mm^2 upwards, in which case only the reduced SNR affects the results with CSF.

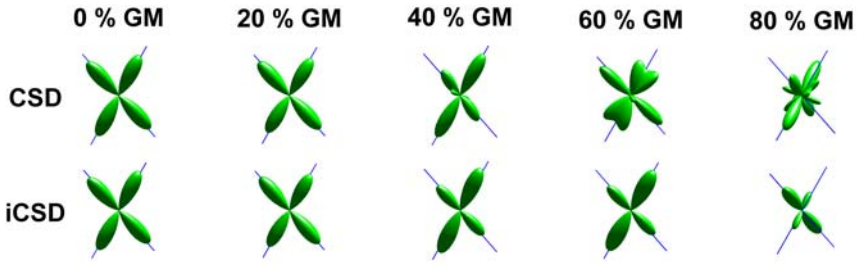

Figure 8: Examples of the fODFs estimated with the iCSD (bottom) and original CSD (top) with different isotropic GM VFs (0 %, 20 %, 40 %, 60 % and 80 %). The blue lines correspond to the correct simulated fiber orientations.

The proposed method takes the isotropic diffusion into account in the RF used in the deconvolution of the fODF from the DW signal. Thus, the results show a more significant improvement with GM PVEs. The proposed method increased the precision of the identified fiber orientations and decreased the number of spurious false peaks in the simulation experiments under GM PVEs. The improvement was clear for diffusion-weightings from 1000 s/mm^2 to 3500 s/mm^2, for maximum SH orders from 8 to 14, for SNRs from 10 to 60, and for angles between the crossing fiber configurations from 50 to 90 degrees. For CSF PVEs, the improvement was generally very small, and more noticeable only in the number of false peaks detected with very low SNRs or very high VFs. Based on the simulation results presented in Figure 5, we suggest to avoid the use of very high SH orders in the estimation of the fODFs with iCSD (or CSD) in regions with significant GM PVEs. The simulation results were not sensitive to differences in the threshold values used in the peak extraction or clustering.

In addition, experiments performed with bootstrapping of the residuals in real data showed a significant increase in the precision of the identified fiber orientations from 25 % GM VF and a significant decrease in the number of detected unstable peaks from 15 % GM VF. No significant improvement was detected with CSF VFs, except for the global reduction in the number of unstable peaks. The similarity between the simulations and the in-vivo experiments was clear.

From Fig. 11 and Fig. 12 it can be observed that in areas with significant PVEs the number of spurious peaks was reduced, similar to what has been observed from the simulation and bootstrapping experiments (Sections 3.1

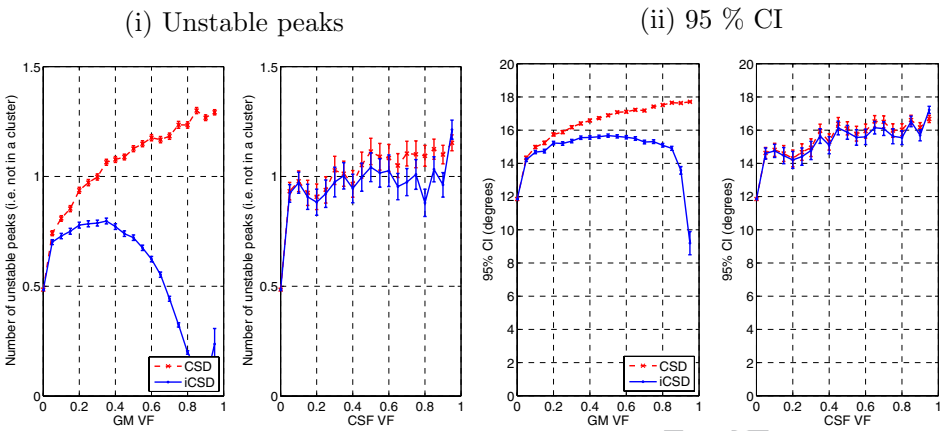

Figure 9: The number of unstable peaks (A) and the precision (95 % CI) of the identified peaks as a function of non-white matter (GM or CSF) volume fraction (VF). Estimated with SH order 8 based on 200 bootstrap realizations in real data with iCSD and original CSD.

and 3.2), and the amplitudes of the fODFs were decreased due to the removal of non-WM signal. The fODFs estimated with iCSD had less spurious peaks and in some cases, they showed a fanning structure of the cortical tract extensions (e.g. in Fig. 12). This kind of fiber dispersion has been previously reported to be present in high-resolution DW-MRI data acquired in the Human Connectome Project and is supported by histology in the macaque brain (Sotiropoulos et al., 2013b,a; Ugurbil et al., 2013; Jeurissen et al., 2014).

The comparison of the tract density images between iCSD and CSD showed increased tract density in the main white matter tracts and their cortical projections and decreased tract density in for example subcortical GM. However, the changes in the tract density were small, so the global tract density remains highly similar to tractography performed based on the original CSD method. This may be due to the improvements being restricted to voxels with non-WM PVEs and thus, the proposed method mostly affects voxels located close to the end-points of the tracts. Although globally the changes are small, the end-points of the tracts will be more correctly reconstructed with iCSD, as shown by the simulations and the bootstrapping experiments, as well as the visualization of estimated fODFs. Accuracy of the end-points of the tracts is especially important in connectomics, in which the connectivity between GM regions is analyzed (Bullmore and Sporns, 2009;

(i) Unstable peaks

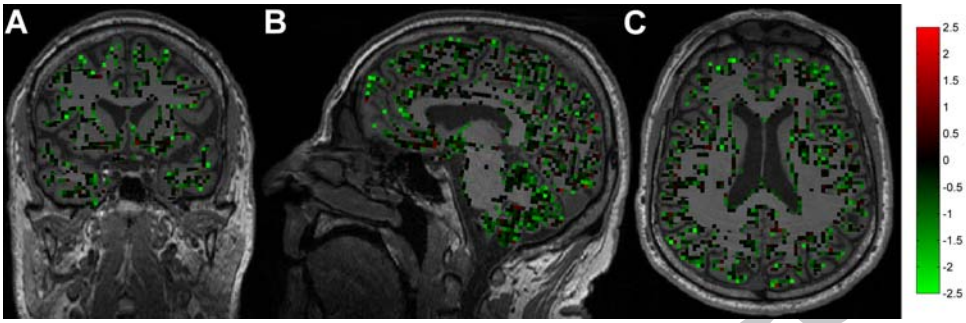

(ii) 95 % CI

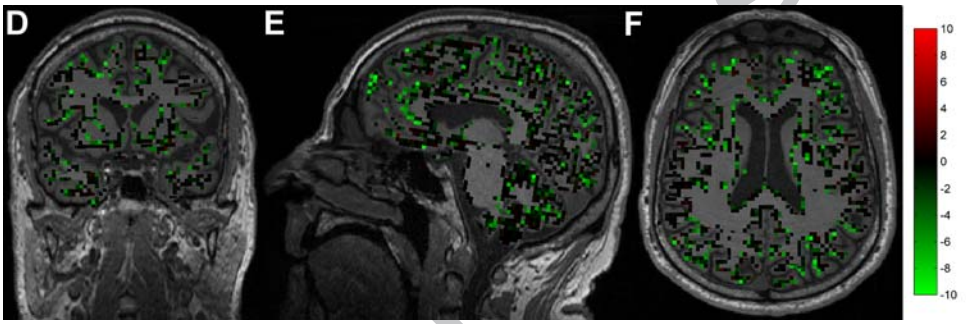

Figure 10: An illustration of coronal (A and D), sagittal (B and E) and axial (C and F) slices showing the spatial distribution of the differences (iCSD – CSD) in the number of unstable peaks (A–C) and in the precision (95 % CI) of the identified fiber orientations (D–E) between iCSD and original CSD. Estimated with SH order 8 based on 200 bootstrap realizations in real data.

Rubinov and Sporns, 2010; Hagmann et al., 2010).

Parker and coworkers previously reported a pitfall in the fiber orientation estimation performed with spherical deconvolution (Parker et al., 2013). They showed that incorrect calibration of the single-fiber RF caused spurious peaks in the fODF. Their findings are closely related to our previous results concerning non-WM PVEs (Roine et al., 2014a). However, while Parker's results arose from incorrect calibration of the WM RF, our previous results concerned isotropic non-WM PVEs assuming that the WM RF was correctly calibrated. The proposed iCSD method accounts for the non-WM PVEs by modifying the RF accordingly, but it uses a traditional WM RF and thus, the pitfall proposed in Parker et al. (2013) is not eliminated. To avoid this

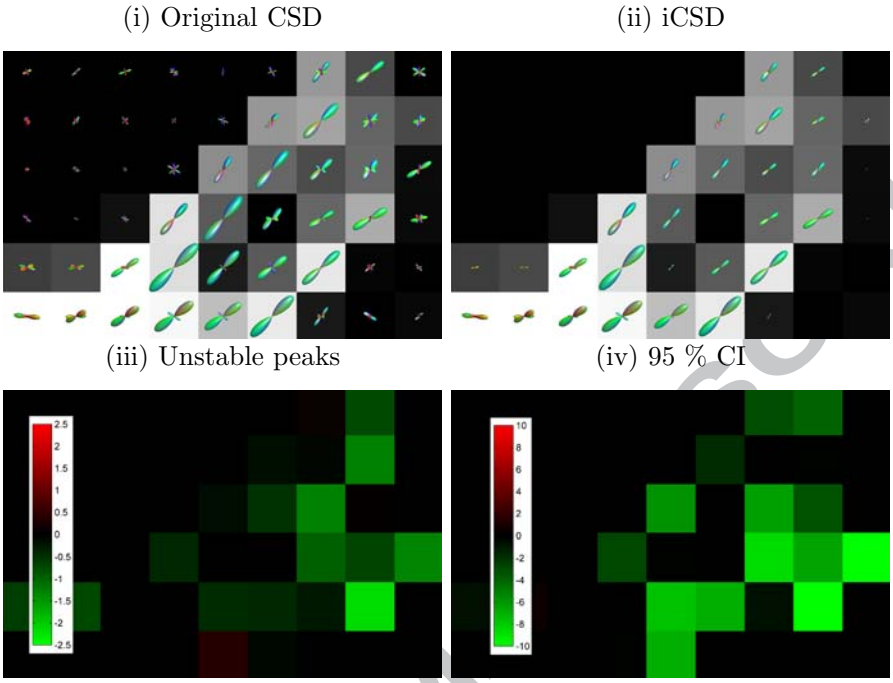

Figure 11: An illustration of fODFs from lateral occipital cortex estimated with original CSD (*i*) and iCSD (*ii*) visualized on the WM volume fraction (VF) map (white = 100 % WM, black = 0% WM). The differences (iCSD – CSD) in the number of unstable peaks (*iii*) and in the precision (95 % CI) of the identified fiber orientations (*iv*) are also presented.

pitfall, we have used state-of-the-art methods to estimate the WM RF and therefore, the calibration of the single-fiber RF is as accurate as possible with the currently available methods.

A limitation of this study is that the in-vivo results can not be validated with a hardware phantom, because no such phantom containing also significant non-WM PVEs exists. Nonetheless, the similarity of the in-vivo results concerning precision of the identified fiber orientations and the number of detected unstable peaks provides further support for the simulation results. Another limitation is that the proposed method depends on the availability of a structural MRI scan aligned with the DW-MRI data. This has two implications. First, it requires that a structural MRI scan of the same subject is available. Second, it requires that the significant EPI distortions typically seen in DW data sets are properly accounted for to be able to align

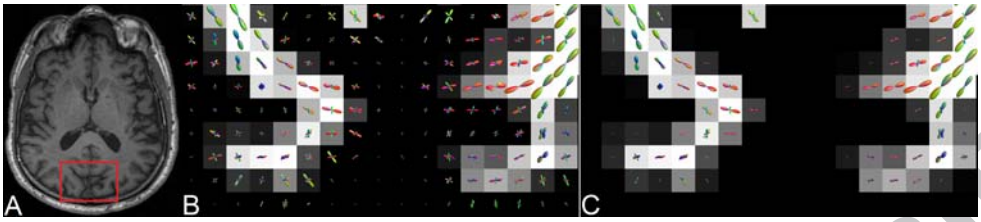

Figure 12: An illustration of fODFs in an example area in the occipital lobe marked with a red rectangle (A). The fODFs were estimated with original CSD (B) and iCSD (C) using SH order 8 and are visualized on the WM volume fraction (VF) map (white = 100 % WM, black = 0% WM).

the DW data accurately with the undistorted structural image. Our current pipeline achieves EPI distortion correction by means of acquiring at least one additional b = 0 s/mm^2 volume with reversed phase encoding (Andersson et al., 2003). If these conditions are not fulfilled, our current pipeline cannot correctly account for isotropic PVEs.

Furthermore, the experiments and the proposed method are currently restricted to the CSD approach, although it may be possible to incorporate a similar approach into other methods. Previous studies indicate that the non-WM PVEs are present in DW-MRI in general (Alexander et al., 2001; Behrens et al., 2007; Pasternak et al., 2009; Dell'Acqua et al., 2010; Metzler-Baddeley et al., 2012b). While some of the analysis methods already account for (Behrens et al., 2003, 2007; Pasternak et al., 2009; Jbabdi et al., 2012) or reduce the adverse effects of these PVEs (Dell'Acqua et al., 2010), many of the currently used methods do not. Dell'Acqua et al. (2010) proposed to use adaptive regularization to damp the spurious peaks caused by the isotropic PVEs in the iterative Richardson-Lucy deconvolution algorithm (Dell'Acqua et al., 2010). The number of spurious false peaks was shown to be reduced, while the angular resolution was preserved. However, their method produces non-zero fiber densities also in the CSF, unlike the proposed iCSD method. In CSD, which is a widely used method (Metzler-Baddeley et al., 2012a; Emsell et al., 2013; Forde et al., 2013; Kristo et al., 2013; McGrath et al., 2013a,b; Reijmer et al., 2013b,a; Thompson et al., 2014; Roine et al., 2014b), the isotropic PVEs were not taken into account earlier.

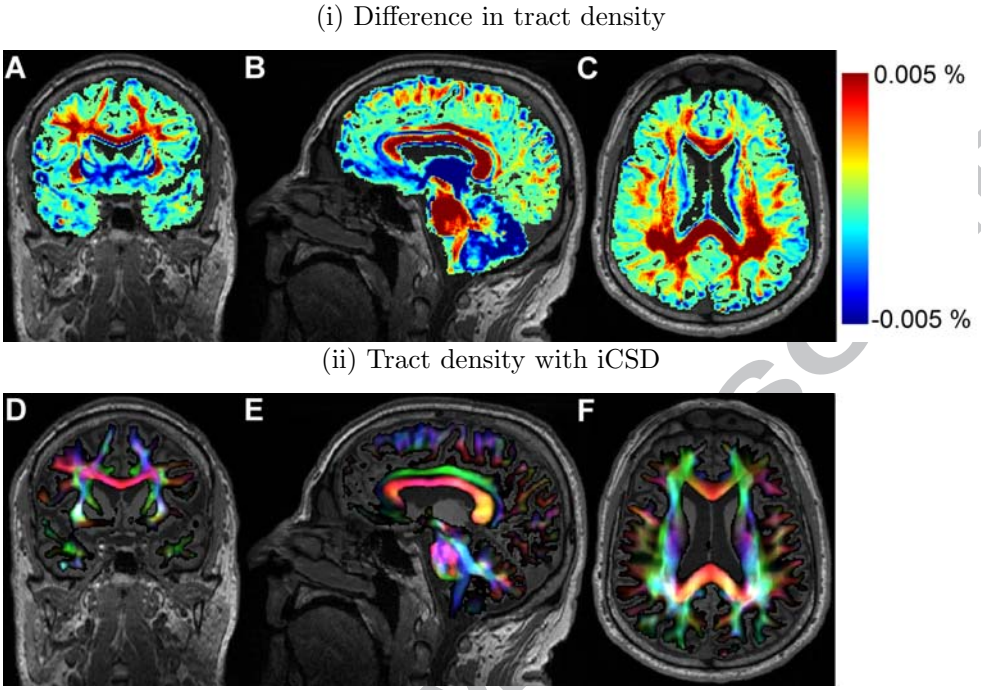

Figure 13: An illustration of coronal (A and D), sagittal (B and E) and axial (C and F) slices showing the differences in the tract density images (iCSD – CSD, as a fraction of the total number of tracts) in A–C and the tract density images of the iCSD method in D–E. Estimated with SH order 8, and probabilistic tractography with the iFOD2 algorithm.

5. Conclusions

We propose a novel method, *informed* CSD (iCSD), in which the single-fiber RF used in the estimation of the fODFs in CSD is modified to account for local tissue VFs estimated from high-resolution anatomical data. Significant improvement in the precision of the estimated fiber orientations and in the number of spurious false peaks detected in GM contaminated regions was shown both with simulated and real DW data. However, neither the proposed iCSD method nor the original CSD method is able to correctly resolve fiber crossing angles of less than 60 degrees under significant non-WM PVEs. The proposed method will be particularly useful in connectomics, where the end-points of the tracts are critical for the successful analysis of connectivity between GM regions.

6. Acknowledgments

This work was supported by the Fund for Scientific Research-Flanders (FWO), and by the Interuniversity Attraction Poles Program (P7/11) initiated by the Belgian Science Policy Office. The research of A.L. is supported by VIDI Grant 639.072.411 from the Netherlands Organisation for Scientific Research (NWO). T.R. received support from the Instrumentarium Scientific Foundation and the Finnish Science Foundation for Economics and Technology.

7. Vitae

Timo Roine received his M.Sc.(Tech.) in 2009 from Helsinki University of Technology (currently Aalto University), Finland. He did research on mineral processing technology in the Control Engineering group of Aalto University from 2005 to 2010. From 2010 to 2012 he worked as a consultant for healthcare management in Nordic Healthcare Group, Finland. In 2012 he started his PhD about diffusion MRI at the iMinds-Vision Lab, Department of Physics, University of Antwerp, Belgium under the supervision of Ben Jeurissen, Alexander Leemans and Jan Sijbers.

Ben Jeurissen received an MSc in Computer Science in 2004 and in Biomedical Imaging in 2006, both from the University of Antwerp, Belgium. In 2012, he obtained a PhD in Science from the University of Antwerp. From 2012, he worked as a post-doctoral researcher in the Vision Lab, at the Physics department of the University of Antwerp and at The Florey Institute of Neuroscience and Mental Health in Melbourne, Australia. He is a Junior Fellow of the International Society of Magnetic Resonance in Medicine and specializes in image processing of diffusion MRI data for investigating microstructural tissue organization.

Daniele Perrone is a PhD candidate in the "Image Processing and Interpretation" research group, at the Department of Telecommunications and Information Processing, Ghent University, Belgium, and part of the Flemish ICT research institute iMinds. His research focuses on modeling and restoration of Diffusion MR images, with special attention to imaging of brain tissue microstructures and connectivity mapping.

Jan Aelterman is a PhD candidate in the "Image Processing and Interpretation" research group, at the Department of Telecommunications and Information Processing, Ghent University, Belgium, and part of the Flemish

ICT research institute iMinds. His research focuses on restoration of natural images, with a focus on reconstruction of MRI images.

In 1989, **Wilfried Philips** received the Diploma degree in electrical engineering and in 1993 the Ph.D. in applied sciences, both from Ghent University, Belgium. From 1989 to 1997 he worked at the Department of Electronics and Information Systems of Ghent University. Since 1997, he has been at the Department of Telecommunications and Information Processing of Ghent University, where he is currently a full-time professor and is heading the research group Image Processing and Interpretation, which is also part of the Flemish ICT research institute iMinds. Wilfried Philips is also a senior member of IEEE.

Alexander Leemans is a physicist who received his PhD in 2006 at the University of Antwerp, Belgium. From 2007 to 2009, he worked as a postdoctoral researcher at the Cardiff University Brain Research Imaging Center (CUBRIC), Cardiff University, Wales, United Kingdom. In 2009, he joined the Image Sciences Institute (ISI), University Medical Center Utrecht, the Netherlands, where he currently holds a tenured faculty position as Associate Professor. His current research interests include modeling, processing, visualizing and analyzing diffusion MRI data for investigating microstructural and architectural tissue organization. He heads the PROVIDI Lab and is the developer of the software ExploreDTI.

Jan Sijbers received the B.Sc. and M.S. degrees in physics from the University of Hasselt and the University of Antwerp in 1991 and 1993, respectively, and the Ph.D. degree in Sciences from the University of Antwerp in 1998, for which he received the FWO Barco Award in 1999. Currently, he is full professor and head of the Vision Lab at the Physics department of the University of Antwerp. His research is focused on biomedical image reconstruction, processing and analysis (mainly in the field of MRI and CT). He has authored more than 150 publications.

References

Alexander, A.L., Hasan, K.M., Lazar, M., Tsuruda, J.S., Parker, D.L., 2001. Analysis of partial volume effects in diffusion-tensor MRI. Magnetic Resonance in Medicine 45, 770–780.

Alexander, D.C., 2005. Maximum entropy spherical deconvolution for diffusion MRI, in: Information Processing in Medical Imaging, Springer. pp. 76–87.

Anderson, A.W., 2005. Measurement of fiber orientation distributions using high angular resolution diffusion imaging. Magnetic Resonance in Medicine 54, 1194–1206.

Andersson, J., Xu, J., Yacoub, E., Auerbach, E., Moeller, S., Ugurbil, K., 2012. A comprehensive gaussian process framework for correcting distortions and movements in diffusion images, in: Proceedings of the 20th Annual Meeting of ISMRM, Melbourne, Australia, p. 2426.

Andersson, J.L., Skare, S., Ashburner, J., 2003. How to correct susceptibility distortions in spin-echo echo-planar images: application to diffusion tensor imaging. NeuroImage 20, 870–888.

Ashburner, J., Friston, K., 2003. Rigid body registration, in: Frackowiak, R., Friston, K., Frith, C., Dolan, R., Friston, K., Price, C., Zeki, S., Ashburner, J., Penny, W. (Eds.), Human Brain Function. 2nd ed.. London: Academic Press, pp. 635–655.

Basser, P.J., Jones, D.K., 2002. Diffusion-tensor MRI: theory, experimental design and data analysisa technical review. NMR in Biomedicine 15, 456–467.

Basser, P.J., Mattiello, J., LeBihan, D., 1994a. Estimation of the effective self-diffusion tensor from the NMR spin echo. Journal of Magnetic Resonance, Series B 103, 247–254.

Basser, P.J., Mattiello, J., LeBihan, D., 1994b. MR diffusion tensor spectroscopy and imaging. Biophysical Journal 66, 259–267.

Basser, P.J., Pajevic, S., 2000. Statistical artifacts in diffusion tensor MRI (DT-MRI) caused by background noise. Magnetic Resonance in Medicine 44, 41–50.

Basser, P.J., Pajevic, S., Pierpaoli, C., Duda, J., Aldroubi, A., 2000. In vivo fiber tractography using DT-MRI data. Magnetic Resonance in Medicine 44, 625–632.

Behrens, T., Berg, H.J., Jbabdi, S., Rushworth, M., Woolrich, M., 2007. Probabilistic diffusion tractography with multiple fibre orientations: What can we gain? NeuroImage 34, 144–155.

Behrens, T., Woolrich, M., Jenkinson, M., Johansen-Berg, H., Nunes, R., Clare, S., Matthews, P., Brady, J., Smith, S., 2003. Characterization and propagation of uncertainty in diffusion-weighted MR imaging. Magnetic Resonance in Medicine 50, 1077–1088.

Bullmore, E., Sporns, O., 2009. Complex brain networks: graph theoretical analysis of structural and functional systems. Nature Reviews Neuroscience 10, 186–198.

Calamante, F., Tournier, J.D., Jackson, G.D., Connelly, A., 2010. Track-density imaging (TDI): super-resolution white matter imaging using whole-brain track-density mapping. NeuroImage 53, 1233–1243.

Canales-Rodríguez, E.J., Iturria-Medina, Y., Alemán-Gómez, Y., Melie-García, L., 2010. Deconvolution in diffusion spectrum imaging. Neuroimage 50, 136–149.

Conturo, T., Lori, N., Cull, T., Akbudak, E., Snyder, A., Shimony, J., McKinstry, R., Burton, H., Raichle, M., 1999. Tracking neuronal fiber pathways in the living human brain, in: Proceedings of the National Academy of Sciences, National Academy of Sciences. pp. 10422–10427.

Daducci, A., Canales-Rodríguez, E., Descoteaux, M., Garyfallidis, E., Gur, Y., Lin, Y., Mani, M., Merlet, S., Paquette, M., Ramirez-Manzanares, A., Reisert, M., Reis Rodrigues, P., Sepehrband, F., Caruyer, E., Choupan, J., Deriche, R., Jacob, M., Menegaz, G., Prkovska, V., Rivera, M., Wiaux, Y., Thiran, J., 2014. Quantitative comparison of reconstruction methods for intra-voxel fiber recovery from diffusion MRI. IEEE transactions on medical imaging 33, 384.

Davison, A., Hinkley, D., 1997. Bootstrap methods and their application. volume 1. Cambridge: Cambridge University Press.

Dell'Acqua, F., Rizzo, G., Scifo, P., Clarke, R.A., Scotti, G., Fazio, F., 2007. A model-based deconvolution approach to solve fiber crossing in diffusion-weighted MR imaging. Biomedical Engineering, IEEE Transactions on 54, 462–472.

Dell'Acqua, F., Scifo, P., Rizzo, G., Catani, M., Simmons, A., Scotti, G., Fazio, F., 2010. A modified damped Richardson–Lucy algorithm to reduce

isotropic background effects in spherical deconvolution. NeuroImage 49, 1446–1458.

Descoteaux, M., Angelino, E., Fitzgibbons, S., Deriche, R., 2007. Regularized, fast, and robust analytical Q-ball imaging. Magnetic Resonance in Medicine 58, 497–510.

Descoteaux, M., Deriche, R., Knosche, T., Anwander, A., 2009. Deterministic and probabilistic tractography based on complex fibre orientation distributions. IEEE Transactions on Medical Imaging 28, 269–286.

Dietrich, O., Raya, J.G., Reeder, S.B., Reiser, M.F., Schoenberg, S.O., 2007. Measurement of signal-to-noise ratios in MR images: Influence of multichannel coils, parallel imaging, and reconstruction filters. Journal of Magnetic Resonance Imaging 26, 375–385.

Emsell, L., Leemans, A., Langan, C., Van Hecke, W., Barker, G.J., McCarthy, P., Jeurissen, B., Sijbers, J., Sunaert, S., Cannon, D.M., McDonald, C., 2013. Limbic and callosal white matter changes in euthymic bipolar i disorder: an advanced diffusion magnetic resonance imaging tractography study. Biological psychiatry 73, 194–201.

Farquharson, S., Tournier, J.D., Calamante, F., Fabinyi, G., Schneider-Kolsky, M., Jackson, G.D., Connelly, A., 2013. White matter fiber tractography: why we need to move beyond DTI: Clinical article. Journal of Neurosurgery 118, 1367–1377.

Forde, N.J., Ronan, L., Suckling, J., Scanlon, C., Neary, S., Holleran, L., Leemans, A., Tait, R., Rua, C., Fletcher, P.C., Jeurissen, B., Dodds, C.M., Miller, S.R., Bullmore, E.T., McDonald, C., Nathan, P.J., Cannon, D.M., 2013. Structural neuroimaging correlates of allelic variation of the BDNF val66met polymorphism. NeuroImage doi:10.1016/j.neuroimage.2013.12.050.

Frank, L.R., 2001. Anisotropy in high angular resolution diffusion-weighted MRI. Magnetic Resonance in Medicine 45, 935–939.

Frank, L.R., 2002. Characterization of anisotropy in high angular resolution diffusion-weighted MRI. Magnetic Resonance in Medicine 47, 1083–1099.

Hagmann, P., Cammoun, L., Gigandet, X., Gerhard, S., Ellen Grant, P., Wedeen, V., Meuli, R., Thiran, J.P., Honey, C.J., Sporns, O., 2010. MR connectomics: principles and challenges. Journal of Neuroscience Methods 194, 34–45.

Hosey, T., Williams, G., Ansorge, R., 2005. Inference of multiple fiber orientations in high angular resolution diffusion imaging. Magnetic Resonance in Medicine 54, 1480–1489.

Jansons, K.M., Alexander, D.C., 2003. Persistent angular structure: new insights from diffusion magnetic resonance imaging data. Inverse problems 19, 1031.

Jbabdi, S., Sotiropoulos, S.N., Savio, A.M., Graña, M., Behrens, T.E., 2012. Model-based analysis of multishell diffusion MR data for tractography: How to get over fitting problems. Magnetic Resonance in Medicine 68, 1846–1855.

Jeurissen, B., Leemans, A., Jones, D.K., Tournier, J.D., Sijbers, J., 2011. Probabilistic fiber tracking using the residual bootstrap with constrained spherical deconvolution. Human Brain Mapping 32, 461–479.

Jeurissen, B., Leemans, A., Tournier, J.D., Jones, D.K., Sijbers, J., 2013. Investigating the prevalence of complex fiber configurations in white matter tissue with diffusion magnetic resonance imaging. Human Brain Mapping 34, 2747–2766.

Jeurissen, B., Tournier, J.D., Dhollander, T., Connelly, A., Sijbers, J., 2014. Multi-tissue constrained spherical deconvolution for improved analysis of multi-shell diffusion MRI data. NeuroImage doi:http://dx.doi.org/10.1016/j.neuroimage.2014.07.061.

Jones, D., Horsfield, M., Simmons, A., 1999. Optimal strategies for measuring diffusion in anisotropic systems by magnetic resonance imaging. Magn Reson Med 42.

Jones, D.K., 2003. Determining and visualizing uncertainty in estimates of fiber orientation from diffusion tensor MRI. Magnetic Resonance in Medicine 49, 7–12.

Jones, D.K., 2008. Studying connections in the living human brain with diffusion MRI. Cortex 44, 936–952.

Jones, D.K. (Ed.), 2010. Diffusion MRI: Theory, Methods, and Applications. Oxford: Oxford University Press.

Jones, D.K., Leemans, A., 2011. Diffusion tensor imaging, in: Modo, M., Bulte, J.W. (Eds.), Magnetic Resonance Neuroimaging. Humana Press. volume 711 of *Methods in Molecular Biology*, pp. 127–144.

Kristo, G., Leemans, A., Raemaekers, M., Rutten, G.J., Gelder, B., Ramsey, N.F., 2013. Reliability of two clinically relevant fiber pathways reconstructed with constrained spherical deconvolution. Magnetic Resonance in Medicine 70, 1544–1556.

Leemans, A., Jeurissen, B., Sijbers, J., Jones, D., 2009. ExploreDTI: a graphical toolbox for processing, analyzing, and visualizing diffusion MR data, in: Proc Intl Soc Mag Reson Med, p. 3536.

Leemans, A., Jones, D.K., 2009. The B-matrix must be rotated when correcting for subject motion in DTI data. Magnetic Resonance in Medicine 61, 1336–1349.

Leemans, A., Sijbers, J., Verhoye, M., Van der Linden, A., , Van Dyck, D., 2005. Mathematical framework for simulating diffusion tensor MR neural fiber bundles. Magnetic Resonance in Medicine 53, 944–953.

Mattiello, J., Basser, P.J., Le Bihan, D., 1997. The b matrix in diffusion tensor echo-planar imaging. Magnetic Resonance in Medicine 37, 292–300.

McGrath, J., Johnson, K., O'Hanlon, E., Garavan, H., Gallagher, L., Leemans, A., 2013a. White matter and visuospatial processing in autism: A constrained spherical deconvolution tractography study. Autism Research 6, 307–319.

McGrath, J., Johnson, K., O'Hanlon, E., Garavan, H., Leemans, A., Gallagher, L., 2013b. Atypical functional connectivity in autism spectrum disorder is associated with disrupted white matter microstructural organisation. Frontiers in Human Neuroscience 7, 434. doi:10.3389/fnhum.2013.00434.

Metzler-Baddeley, C., Hunt, S., Jones, D.K., Leemans, A., Aggleton, J.P., O'Sullivan, M.J., 2012a. Temporal association tracts and the breakdown of episodic memory in mild cognitive impairment. Neurology 79, 2233–2240.

Metzler-Baddeley, C., O'Sullivan, M.J., Bells, S., Pasternak, O., Jones, D.K., 2012b. How and how not to correct for CSF-contamination in diffusion MRI. NeuroImage 59, 1394–1403.

Mori, S., van Zijl, P., 2002. Fiber tracking: principles and strategiesa technical review. NMR in Biomedicine 15, 468–480.

Mugler, J.P., Brookeman, J.R., 1990. Three-dimensional magnetization-prepared rapid gradient-echo imaging (3D MP RAGE). Magnetic Resonance in Medicine 15, 152–157.

Parker, G.D., Marshall, D., Rosin, P.L., Drage, N., Richmond, S., Jones, D.K., 2013. A pitfall in the reconstruction of fibre ODFs using spherical deconvolution of diffusion MRI data. NeuroImage 65, 433–448.

Pasternak, O., Sochen, N., Gur, Y., Intrator, N., Assaf, Y., 2009. Free water elimination and mapping from diffusion MRI. Magnetic Resonance in Medicine 62, 717–730.

Patenaude, B., Smith, S.M., Kennedy, D.N., Jenkinson, M., 2011. A Bayesian model of shape and appearance for subcortical brain segmentation. NeuroImage 56, 907–922.

Reijmer, Y.D., Freeze, W.M., Leemans, A., Biessels, G.J., 2013a. The effect of lacunar infarcts on white matter tract integrity. Stroke doi:10.1161/STROKEAHA.113.001321.

Reijmer, Y.D., Leemans, A., Brundel, M., Kappelle, L.J., Biessels, G.J., et al., 2013b. Disruption of the cerebral white matter network is related to slowing of information processing speed in patients with type 2 diabetes. Diabetes 62, 2112–2115.

Roine, T., Jeurissen, B., Perrone, D., Aelterman, J., Leemans, A., Philips, W., Sijbers, J., 2014a. Isotropic non-white matter partial volume effects in constrained spherical deconvolution. Frontiers in Neuroinformatics 8, 28. doi:10.3389/fninf.2014.00028.

Roine, U., Salmi, J., Roine, T., Nieminen-von Wendt, T., Leppämäki, S., Rintahaka, P., Tani, P., Leemans, A., Sams, M., 2014b. Constrained spherical deconvolution-based tractography and tract-based spatial statistics show abnormal microstructural organization in Asperger syndrome. Molecular Autism In press.

Rubinov, M., Sporns, O., 2010. Complex network measures of brain connectivity: uses and interpretations. NeuroImage 52, 1059–1069.

Schultz, T., Westin, C.F., Kindlmann, G., 2010. Multi-diffusion-tensor fitting via spherical deconvolution: a unifying framework, in: Medical Image Computing and Computer-Assisted Intervention–MICCAI 2010. Springer, pp. 674–681.

Smith, R.E., Tournier, J.D., Calamante, F., Connelly, A., 2012. Anatomically-constrained tractography: Improved diffusion MRI streamlines tractography through effective use of anatomical information. NeuroImage 62, 1924–1938.

Smith, S.M., 2002. Fast robust automated brain extraction. Human Brain Mapping 17, 143–155.

Sotiropoulos, S.N., Chen, C., Dikranian, K., Jbabdi, S., Behrens, T., Van Essen, D.C., Glasser, M.F., 2013a. Comparison of diffusion MRI predictions and histology in the macaque brain, in: Proceedings of the International Society for Magnetic Resonance in Medicine (ISMRM) Annual Meeting, Salt Lake City, p. 835.

Sotiropoulos, S.N., Jbabdi, S., Xu, J., Andersson, J.L., Moeller, S., Auerbach, E.J., Glasser, M.F., Hernandez, M., Sapiro, G., Jenkinson, M., Feinberg, D.A., Yacoub, E., Lenglet, C., Essen, D.C.V., Ugurbil, K., Behrens, T.E., 2013b. Advances in diffusion MRI acquisition and processing in the human connectome project. NeuroImage 80, 125–143. doi:http://dx.doi.org/10.1016/j.neuroimage.2013.05.057.

Stejskal, E., Tanner, J., 1965. Spin diffusion measurements: spin echoes in the presence of a time-dependent field gradient. The Journal of Chemical Physics 42, 288.

Tax, C.M., Jeurissen, B., Vos, S.B., Viergever, M.A., Leemans, A., 2014. Recursive calibration of the fiber response function for spherical deconvolution of diffusion MRI data. NeuroImage 86, 67–80.

Thompson, D.K., Thai, D., Kelly, C.E., Leemans, A., Tournier, J.D., Kean, M.J., Lee, K.J., Inder, T.E., Doyle, L.W., Anderson, P.J., Hunt, R.W., 2014. Alterations in the optic radiations of very preterm childrenperinatal predictors and relationships with visual outcomes. NeuroImage: Clinical 4, 145–153.

Tournier, J., Calamante, F., Connelly, A., 2007. Robust determination of the fibre orientation distribution in diffusion MRI: non-negativity constrained super-resolved spherical deconvolution. NeuroImage 35, 1459–1472.

Tournier, J., Calamante, F., Connelly, A., 2010. Improved probabilistic streamlines tractography by 2nd order integration over fibre orientation distributions, in: Proc. 18th Annual Meeting of the Intl. Soc. Mag. Reson. Med.(ISMRM), p. 1670.

Tournier, J., Calamante, F., Connelly, A., 2012. MRtrix: Diffusion tractography in crossing fiber regions. International Journal of Imaging Systems and Technology 22, 53–66.

Tournier, J., Calamante, F., Connelly, A., et al., 2013. Determination of the appropriate b value and number of gradient directions for high-angular-resolution diffusion-weighted imaging. NMR in Biomedicine 26, 1775–1786.

Tournier, J., Calamante, F., Gadian, D.G., Connelly, A., 2004. Direct estimation of the fiber orientation density function from diffusion-weighted MRI data using spherical deconvolution. NeuroImage 23, 1176–1185.

Tournier, J., Mori, S., Leemans, A., 2011. Diffusion tensor imaging and beyond. Magnetic Resonance in Medicine 65, 1532–1556.

Tournier, J., Yeh, C.H., Calamante, F., Cho, K.H., Connelly, A., Lin, C.P., 2008. Resolving crossing fibres using constrained spherical deconvolution: validation using diffusion-weighted imaging phantom data. NeuroImage 42, 617–625.

Tuch, D.S., 2004. Q-ball imaging. Magnetic Resonance in Medicine 52, 1358–1372.

Tuch, D.S., Reese, T.G., Wiegell, M.R., Makris, N., Belliveau, J.W., Wedeen, V.J., 2002. High angular resolution diffusion imaging reveals intravoxel white matter fiber heterogeneity. Magnetic Resonance in Medicine 48, 577–582.

Ugurbil, K., Xu, J., Auerbach, E.J., Moeller, S., Vu, A.T., Duarte-Carvajalino, J.M., Lenglet, C., Wu, X., Schmitter, S., de Moortele, P.F.V., Strupp, J., Sapiro, G., Martino, F.D., Wang, D., Harel, N., Garwood, M., Chen, L., Feinberg, D.A., Smith, S.M., Miller, K.L., Sotiropoulos, S.N., Jbabdi, S., Andersson, J.L., Behrens, T.E., Glasser, M.F., Essen, D.C.V., Yacoub, E., 2013. Pushing spatial and temporal resolution for functional and diffusion MRI in the Human Connectome Project. NeuroImage 80, 80–104.

Vos, S.B., Jones, D.K., Viergever, M.A., Leemans, A., 2011. Partial volume effect as a hidden covariate in DTI analyses. NeuroImage 55, 1566–1576.

Wedeen, V., Hagmann, P., Tseng, W., Reese, T., Weisskoff, R., 2005. Mapping complex tissue architecture with diffusion spectrum magnetic resonance imaging. Magnetic Resonance in Medicine 54, 1377–1386.

Wedeen, V.J., Wang, R., Schmahmann, J.D., Benner, T., Tseng, W., Dai, G., Pandya, D., Hagmann, P., D'Arceuil, H., de Crespigny, A.J., 2008. Diffusion spectrum magnetic resonance imaging (DSI) tractography of crossing fibers. NeuroImage 41, 1267–1277.

Zhang, Y., Brady, M., Smith, S., 2001. Segmentation of brain MR images through a hidden Markov random field model and the expectation-maximization algorithm. Medical Imaging, IEEE Transactions on 20, 45–57.

Zhou, Q., Michailovich, O., Rathi, Y., 2014. Resolving complex fibre architecture by means of sparse spherical deconvolution in the presence of isotropic diffusion, in: SPIE Medical Imaging, International Society for Optics and Photonics. pp. 903425–903425.

Graphical Abstract

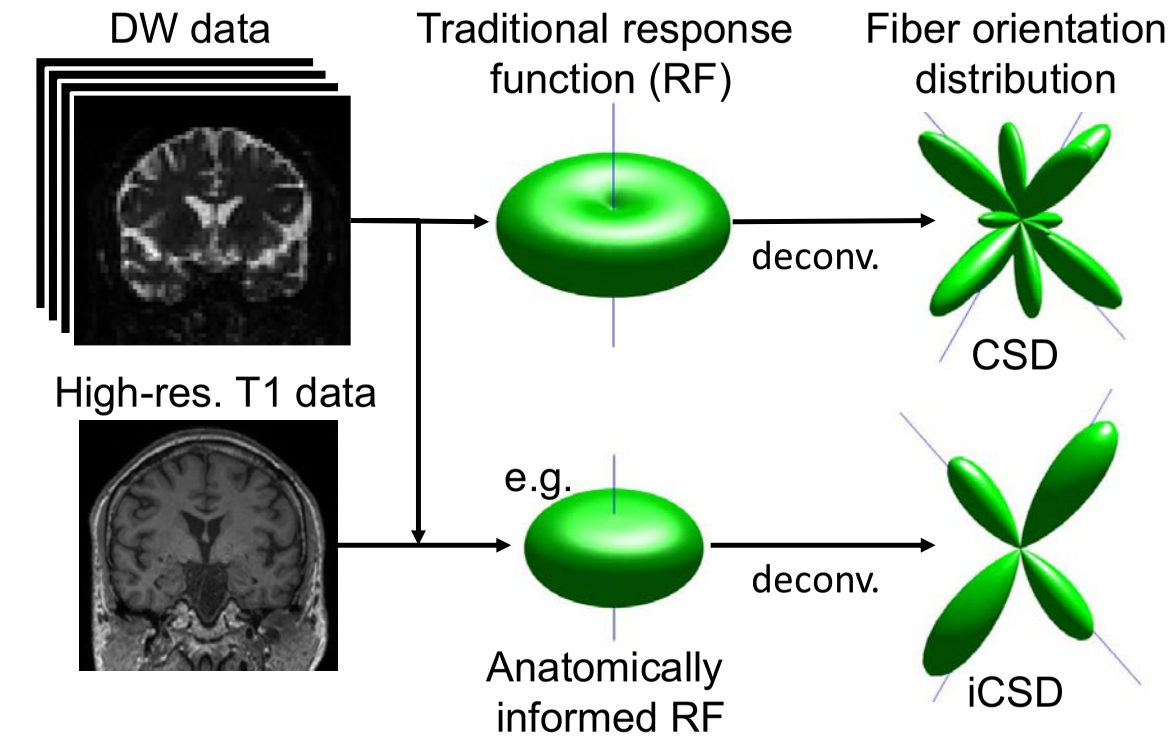

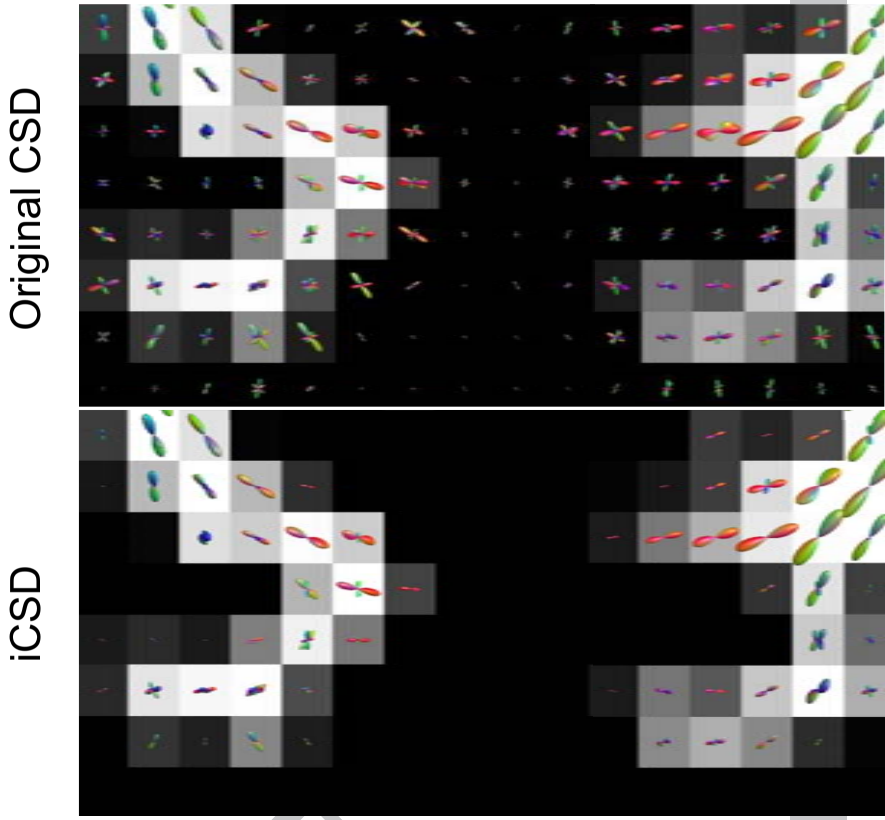

Highlights

- An anatomically-informed approach to estimate fiber orientations with CSD
- Tissue volume fractions are incorporated into the single-fiber response function
- Improved fiber orientation estimation under non-white matter partial volume effects
- Increased the precision of the estimation and reduced the number of spurious peaks